

Simulating Radiative Magneto-convection in the Solar Photosphere

Alexander Vögler

Max-Planck-Institut für Sonnensystemforschung¹
37191 Katlenburg-Lindau, Germany
avoegler@linmpi.mpg.de

Abstract

Magneto-convection, the interaction of a magnetic field with convection in a plasma, plays an important role in many astrophysical systems. Owing to its proximity, the Sun represents the ideal testbed for studies of astrophysical magneto-convection. Realistic numerical simulations of solar magneto-convection are an important complement to solar observations and can contribute to our understanding of magneto-convective processes in the astrophysical context. In this contribution, the MURaM code, a 3D MHD code tailored to applications in the solar photosphere and convection zone, is presented. We give a description of the equations and numerical methods and show the results of the simulation of a solar plage region. Morphology, time evolution and statistical properties of the magnetic field are discussed, and the relation between field strength and brightness of magnetic structures is studied. We briefly discuss the dependence of photospheric magneto-convection on the average magnetic field strength.

1 Introduction

The variety of physical processes resulting from the interaction between convectively driven flows and a magnetic field in an electrically well-conducting fluid is commonly summarized under the term “magneto-convection”. While magneto-convective processes play an important role in many astrophysical phenomena, like the activity of cool stars with an outer convection zone or accretion phenomena in connection with star formation, compact objects, and active galactic nuclei, the Sun is unique in that it is the only astrophysical object on which these processes can (in principle, at least) be observed on their intrinsic spatial and temporal scales. Such processes involve the *generation* of magnetic flux by self-excited dynamo mechanisms, its spatial *distribution* and the formation of intermittent structures by means of flux expulsion, the *dynamics* originating from instabilities, wave excitation, and magnetic reconnection, and the *energetics* due to non-thermal heating and the interference of the magnetic field with convective energy transport.

¹formerly: Max-Planck-Institut für Aeronomie

While the progress in observational techniques like infrared spectroscopy, speckle polarimetry, or adaptive optics has greatly improved our knowledge of photospheric magnetic fields, observations are subject to fundamental limitations with respect to spatial and temporal resolution. Furthermore, they provide information about the variation of physical quantities along the line of sight only in highly convoluted form, while subphotospheric layers are entirely inaccessible to direct observations. Numerical simulations of MHD processes in the photosphere, on the other hand, allow us to obtain information on the full three-dimensional structure of magnetic field configurations, as well as on spatial scales which are not resolved by current observations, thus helping to develop consistent models of the physical processes underlying the observed phenomena. Two main approaches are pursued in the field of magneto-convective simulations: While idealized simulations of simplified model problems allow to study relevant processes in isolation and are amenable to analytical tools like stability analysis and bifurcation theory (see Proctor & Weiss 1982, Proctor 1992, and Weiss 1997 for detailed reviews), “realistic” simulations include elaborate physics like radiative transfer and partial ionization in order to approximate solar conditions. Analysis of realistic numerical models with spectral line and polarization diagnostics allow for a direct comparison with observations. Reviews of realistic simulations of solar magneto-convection have been given by Schüssler (2001) and Schüssler & Knölker (2001).

The simulations presented in this contribution were carried out with the MURaM code, a code suited for realistic MHD simulations in the photosphere, which has recently been developed in a cooperation between the MHD simulation groups at MPS (Katlenburg-Lindau) and at the University of Chicago. After a brief description of the equations and numerical methods employed by our code (Sect. 2), we present the simulation of a solar plage region and discuss morphology, time evolution and statistical properties of the magnetic field as well as the relation between field strength and brightness of magnetic structures (Sect. 3). A brief survey of the different regimes of magneto-convection as obtained from our simulations concludes this contribution (Sect. 4).

2 Equations and Numerical Methods

2.1 The MHD equations

The equations of (non-ideal) MHD are solved in three spatial dimensions in an inertial frame of reference with constant gravitational acceleration, using cartesian coordinates. Writing the system of magnetohydrodynamic equations in conservative form, one has the continuity equation,

$$\frac{\partial \rho}{\partial t} + \nabla \cdot (\rho \mathbf{u}) = 0, \quad (1)$$

the equation of motion,

$$\frac{\partial \rho \mathbf{u}}{\partial t} + \nabla \cdot \left[\rho \mathbf{u} \mathbf{u} + \left(p + \frac{|\mathbf{B}|^2}{8\pi} \right) \mathbf{1} - \frac{\mathbf{B}\mathbf{B}}{4\pi} \right] = \rho \mathbf{g} + \nabla \cdot \underline{\underline{\tau}}, \quad (2)$$

the energy equation,

$$\begin{aligned} \frac{\partial e}{\partial t} + \nabla \cdot \left[\mathbf{u} \left(e + p + \frac{|\mathbf{B}|^2}{8\pi} \right) - \frac{1}{4\pi} \mathbf{B}(\mathbf{u} \cdot \mathbf{B}) \right] \\ = \frac{1}{4\pi} \nabla \cdot (\mathbf{B} \times \eta \nabla \times \mathbf{B}) + \nabla \cdot (\mathbf{u} \cdot \underline{\underline{\tau}}) + \nabla \cdot (K \nabla T) \\ + \rho (\mathbf{g} \cdot \mathbf{u}) + Q_{\text{rad}}, \end{aligned} \quad (3)$$

and the induction equation,

$$\frac{\partial \mathbf{B}}{\partial t} + \nabla \cdot (\mathbf{u}\mathbf{B} - \mathbf{B}\mathbf{u}) = -\nabla \times (\eta \nabla \times \mathbf{B}). \quad (4)$$

Here ρ is the mass density, \mathbf{u} the flow velocity, \mathbf{B} the magnetic field and $e = e_{\text{int}} + e_{\text{kin}} + e_{\text{mag}}$ the total energy density per volume, i.e., the sum of internal, kinetic and magnetic energy densities. p is the gas pressure, T is the temperature, \mathbf{g} the vector of gravitational acceleration, and Q_{rad} the radiative source term which is discussed in detail in Sec. 2.3, η is the (constant) magnetic diffusivity, $\underline{\underline{\tau}}$ the viscous stress tensor and K the thermal conductivity. In order to close the system of MHD equations, an equation of state which determines the dependence of pressure, p , and temperature, T , from ρ and e_{int} needs to be specified. At temperatures typically encountered in the photosphere and convection zone, the solar plasma is partly ionized and the simple thermodynamical relations for an ideal gas do not apply. As a consequence of partial ionization, up to 2/3 of the total enthalpy flux is transported by latent heat and bouyancy driving of convective motions is strongly enhanced (Rast & Toomre 1993, Rast et al. 1993). We take into account the first ionization of the eleven most abundant elements in the Sun (which is sufficient for the conditions encountered in the photosphere and uppermost part of the convection zone). The resulting relations are stored in tables from which the required quantities are interpolated during a simulation run.

The system of equations (1)-(4) is solved on a three-dimensional cartesian grid. The spatial derivatives are discretized using 4th order centered differences on a 5^3 point stencil. The code is parallelized by means of domain decomposition. The computational domain is decomposed into a three dimensional array of rectangular subdomains, each of which is equipped with two layers of ghost cells at each of its boundaries, as required by the 4th-order scheme. Time stepping is explicit, using a 4th-order Runge-Kutta solver. In order to stabilize the scheme, shock-resolving diffusion and hyperdiffusivities (Caunt & Korpi 2001) are included which prevent the build-up of energy at scales comparable to the size of the grid cells while leaving well-resolved structures largely unaffected.

2.2 Boundary conditions

The bottom boundary conditions implemented in our code permit free in- and outflow of matter and maintain a constant mass in the computational box as well as a fixed energy flux through the system. In the present version of the code, the top of the domain is closed with stress-free boundary conditions for the horizontal velocity components; the implementation of a more realistic transmitting boundary is under development. The magnetic field is assumed to be vertical at the top and bottom boundary. The horizontal directions are taken to be periodic in all variables.

2.3 Radiative transfer

The photosphere is the region where most of the radiation leaves the Sun and where radiation takes over from convection as the dominant energy transport mechanism. The energy exchange between gas and radiation determines the outgoing radiation intensity as well as the temperature structure of the photosphere and is responsible for the strong changes in entropy which act as the main driver of convection. Therefore, the radiative energy exchange rate, Q_{rad} , is crucial both for the dynamics and for the diagnostics of magneto-convection. Since the mean free path of photons becomes large as the atmosphere becomes transparent in the photosphere, radiative transfer at this height is essentially non-local, rendering the diffusion approximation of radiative energy transport inadequate. Hence, an accurate calculation of Q_{rad} requires the solution of the (time-independent) radiative transfer equation

$$\frac{dI_\nu}{d\tau_\nu} = S_\nu - I_\nu \quad (5)$$

for a number of frequencies and ray directions. I_ν is the (spectral) specific intensity, S_ν is the source function and $d\tau_\nu = \kappa_\nu \rho ds$ is the optical thickness of path element ds . κ_ν is the opacity of the material. We neglect departures from local thermal equilibrium (LTE) and assume that the source function is given by the Planck function, $S_\nu = B_\nu$. Once the radiation field is known, the radiative energy flux,

$$\mathbf{F}_\nu = \int_{4\pi} I_\nu(\boldsymbol{\mu}) \boldsymbol{\mu} d\omega, \quad (6)$$

and the average intensity,

$$J_\nu = \frac{1}{4\pi} \int_{4\pi} I_\nu(\boldsymbol{\mu}) d\omega, \quad (7)$$

can be calculated, where $\boldsymbol{\mu}(\omega)$ is the unit vector pointing in the ray direction. The radiative heating rate then follows from

$$Q_{\text{rad}} = - \int_\nu (\nabla \cdot \mathbf{F}_\nu) d\nu = 4\pi \rho \int_\nu \kappa_\nu (J_\nu - B_\nu) d\nu. \quad (8)$$

Since spectral lines have a significant influence on the energy balance and temperature structure of the upper photosphere, the frequency-dependence of the radiative transfer must be accounted for in order to obtain accurate radiative heating rates. To this end, we use the multigroup method (Nordlund 1982, Ludwig 1992, Vögler et al. 2004), which captures the essential effects of line opacities while keeping the radiative transfer numerically tractable. The basic idea of the multigroup approach is to sort frequencies into groups (typically 4 – 6) according to the height at which they mainly contribute to the radiative heating rate. Since the contribution is strongest where the transition from optically thick to optically thin takes place, an appropriate sorting criterion is the geometrical depth in a 1D reference atmosphere at which optical depth $\tau_\nu = 1$ is reached. For each frequency group an average opacity is defined and a transfer equation

for the group-integrated intensity with a group-integrated source function is solved. A comprehensive description of our multigroup implementation is given by Vögler et al. (2004).

We use an angular resolution of 24 ray directions with 3 directions per octant. The radiative transfer equation (5) is solved for each frequency group and each direction using the short characteristics scheme (Kunasz & Auer 1988) with linear interpolation of opacity, source function, and density along the ray segments within a given grid cell together with bilinear interpolation of the incoming intensity on cell boundaries.

In the context of the domain decomposition used for parallelization, the short characteristics scheme requires an iteration for each ray direction and each frequency group. For a given ray direction the scheme starts in each subdomain at those boundaries through which the radiation enters (the 'upwind' boundaries). The intensity values at these boundaries are assumed to be known. Then the traversal of the subdomain proceeds in the downwind direction, systematically moving away from the upwind boundaries, thus making sure that the upwind intensities can always be determined by interpolation. However, on those upwind boundaries of a subdomain which do not coincide with the top or bottom boundary of the computational box, the intensities are a priori unknown. Therefore, the scheme is iterated until convergence at the boundaries is obtained. After each iteration the intensities at a given upwind boundary are updated with the new values provided by the neighbouring subdomain. We found that 2 – 3 iteration steps per set and direction are usually sufficient, if one chooses as initial guess for the intensities on the upwind boundaries a linear extrapolation of the values of the previous two time steps.

3 Simulation of a solar plage region

In this section we show some results of the simulation of a typical solar plage region. The simulations are part of a parameter study to investigate the properties of photospheric magneto-convection and their dependence on the

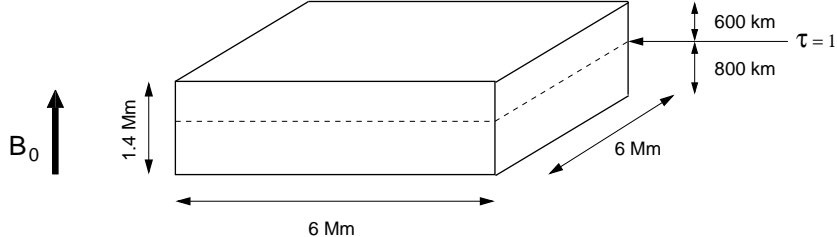


Figure 1: Geometrical setup of the simulation run. The vector \mathbf{B}_0 indicates the vertical homogeneous magnetic field introduced into the hydrodynamic convection at the beginning of the magnetic phase.

average magnetic field strength.

The dimensions of the computational domain are 1400 km in the vertical direction and 6000 km in both horizontal directions, with a resolution of $100 \times 288 \times 288$ grid points. Initially, the simulation was set up as purely hydrodynamical convection, starting from a plane-parallel model of the solar atmosphere extending from 800 km below to 600 km above the level of continuum optical depth unity at 500 nm, as initial condition. After convection has fully developed, a homogeneous vertical initial magnetic field of 200 G, corresponding to the average field strength in a strong solar plage region, is introduced.

3.1 Morphology and statistical properties

Within a few minutes (approximately one turnover time of the convection) after the magnetic field has been introduced, the convective motions transport most of the magnetic flux into the intergranular downflow regions. During this initial phase the magnetic field forms a network structure with maximum field strengths around 2000 G a height of $z = 0$, roughly corresponding to the level of the visible surface, $\langle \tau_{500} \rangle = 1$. The magnetic network is organized on a “mesoscale”, which typically comprises 4-6 granules. As the simulation develops in time, this mesoscale-network turns out to be long-lived with a typical timescale of hours in contrast to the granule lifetime of approximately 10 min. The occurrence of a mesoscale structure, the origin of which is not yet fully understood, is a common and robust feature of many convection simulations. It is observed in both idealized and realistic cases and seems to be largely unaffected by the details of such simulations (see e.g. Cattaneo et al. 2001).

Fig. 2 shows a map of the frequency-integrated emergent intensity (brightness) together with horizontal slices of temperature, vertical magnetic field, and vertical velocity at $z = 0$ for a snapshot taken after about two hours of simulated solar time after the start of the magnetic phase. The magnetic field forms elongated, sheet-like structures that extend along intergranular lanes as well as larger structures, comparable to small pores (“micropores”) on the

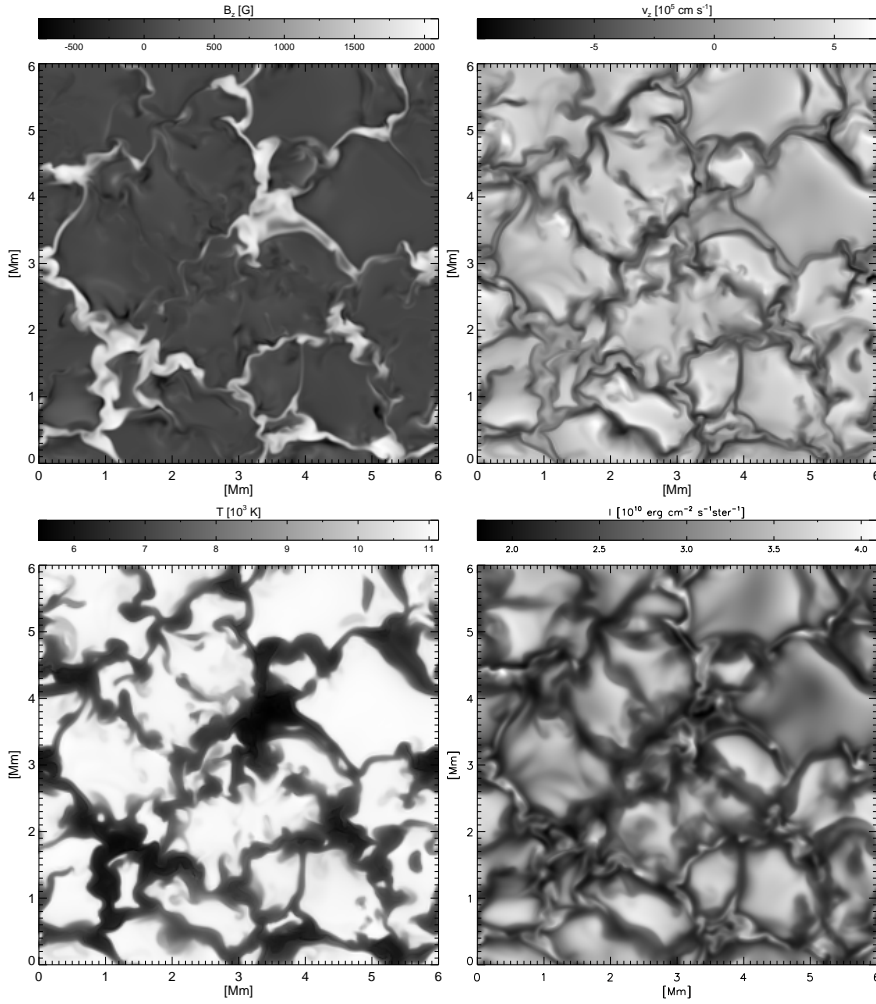


Figure 2: Map of brightness (lower right) and horizontal cuts at the the average geometrical height corresponding to optical depth unity of (clockwise from bottom left) temperature, vertical magnetic field and vertical velocity. The “mesoscale” network of magnetic field structures is embedded in the network of granular downflows. Larger field concentrations appear dark, while the brightness of small magnetic structures occasionally exceeds the brightness of granules. Most of the domain exhibits “abnormal” granulation with small granules (compared to the “normal” granules in the upper right corner).

sun, which are located at vertices where several downflow lanes merge and reach a size of up to 1000 km. The micropores appear dark in the intensity picture, while smaller structures are usually brighter than the non-magnetic downflow lanes, their brightness occasionally exceeding the brightness of granules. A large part of the simulated area shows “abnormal” granulation (Dunn & Zirker 1973) with reduced granule sizes compared to the “normal” granules in the upper right corner of the intensity map. The small pores are far from homogeneous; they show considerable small scale intensity fluctuations which are related to localized upflows in regions of reduced field strength. While the overall shape of the magnetic mesoscale network is stable, the magnetic features show a strong time dependence on small scales as magnetic flux is incessantly redistributed within the network. Consequently, the typical lifetime of the micropores is smaller than the timescale associated to the mesogranular length-scale and is comparable to the granule lifetime. The magnetic network itself is embedded in the network of granular downflows. While convective motions are effectively suppressed inside strong field features, downflows occur at their edges. Basically, this confirms the result of earlier MHD simulations (e.g. Deinzer et al. 1984a,b, Knölker et al. 1991), that influx radiation into a magnetic element drives a baroclinic flow in form of a strong downflow jet at its edge; it is also consistent with the observational finding that observed Stokes-V profiles in plage regions show a distinct area asymmetry in combination with a negligible redshift of the zero-crossing wavelength, a fact which can be understood in terms of non-magnetic downflows adjacent to static magnetic fields (Solanki 1989, Grossmann-Doerth et al. 1989, Sigwarth et al. 1999).

Fig. 3 shows some statistical properties of a layer of 100 km thickness around $\langle \tau_{500} \rangle = 1$. The probability distribution function (PDF) for the magnetic field, multiplied with the sign of its vertical component is shown in the upper left panel. There appears to be a superposition of two components. Most of the volume considered is occupied by weak field, the probability density dropping off approximately exponentially with increasing field strength. The distribution reveals a pronounced local minimum at $B = 0$, indicating that magnetic fields, albeit mostly weak, permeate the whole volume, and *field free* regions are avoided. Superimposed on this exponential distribution is a Gaussian “bulge” (the high field strength wing showing the characteristic parabolic shape on a logarithmic scale) with a maximum around 1500 G, which reflects the sheet- and pore-like structures in the network of concentrated magnetic field.

The joint probability distribution function (joint PDF) of magnetic field strength and inclination angle of the field vector with respect to the horizontal plane given in the upper right panel shows that most of the strong field above the kilogauss level is vertical and upward directed (which is the orientation of the homogeneous initial field), presumably as the result of buoyancy forces acting on the partially evacuated magnetic structures. The inclination angle of weak fields is much more evenly distributed. With decreasing field strength a slight preference for upward directed fields is observed.

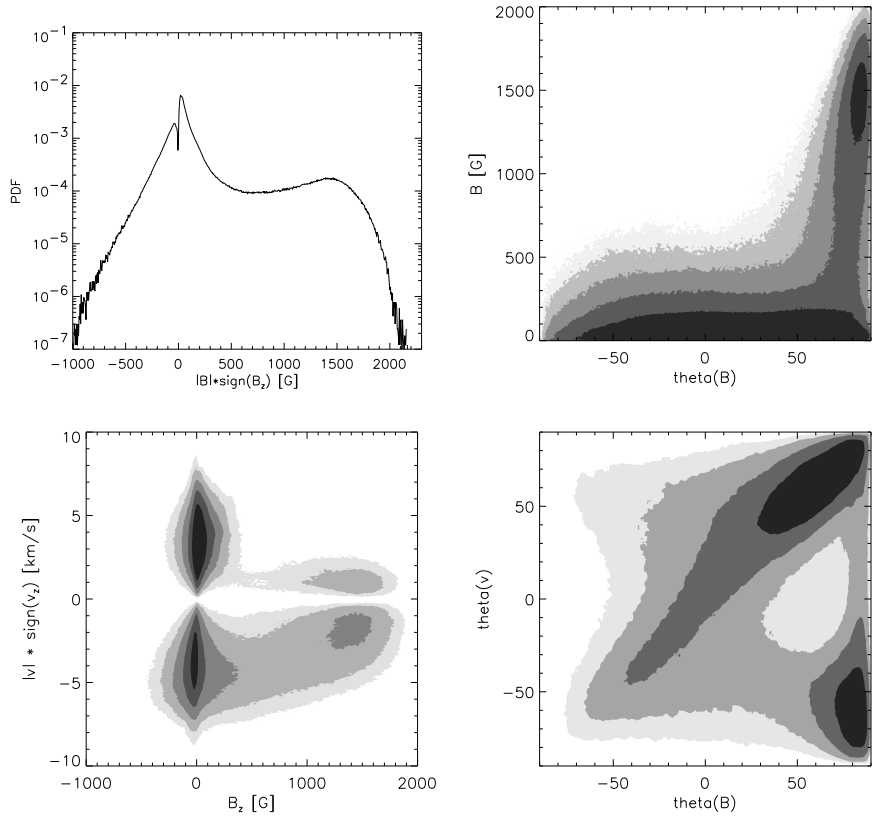


Figure 3: Statistical properties of a layer of 100 km thickness around optical depth unity. Upper left: probability distribution (PDF) of the field strength, signed with the vertical orientation of the field vector. Upper right: joint PDF of field strength and the inclination angle of \mathbf{B} with respect to the horizontal, $\text{theta}(\mathbf{B})$. Lower left: joint PDF of flow velocity, multiplied with the sign of its vertical orientation, and field strength. Lower right: joint PDF of the inclination angles of the flow, $\text{theta}(\mathbf{v})$, and of the magnetic field, $\text{theta}(\mathbf{B})$. The grey-scaling indicates the probability density, with intervals of 0.5 on the \log_{10} scale between greyscale levels.

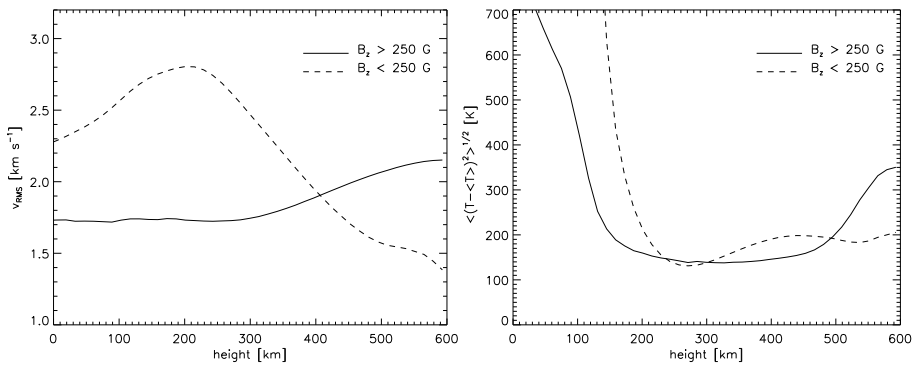


Figure 4: Left panel: rms horizontal velocity in regions of strong and weak magnetic field as function of height. Right panel: rms temperature fluctuations inside and outside strong field regions.

The joint PDF of the vertical magnetic field and the flow velocity signed with the vertical orientation of the flow in the lower left panel (positive velocities correspond to upflows) shows the effect of strong fields on the fluid motions: while flow velocities up to 8 km s^{-1} can be found in weak field regions, the amplitudes of fluid motions are reduced in magnetic structures with field strengths above 1000 G . Fluid motions are not completely suppressed, however, since the predominantly vertical fields leave vertical fluid motions largely unaffected. Downflows are preferred inside strong field features.

The lower right panel of Fig. 3 shows the joint PDF of the inclination angles of magnetic field vector and flow vector with respect to the horizontal plane. The pronounced diagonal lobe indicates that in most of the volume considered flow field and magnetic field are more or less aligned. In addition to this component, one observes a strong correlation of (strong) vertical magnetic field with downflows.

In the upper part of the computational domain, the structure of horizontal flows undergoes a characteristic change with height. This is illustrated by Fig. 4, which shows horizontally averaged (root-mean-square) velocities of horizontal flows (left panel) and horizontal rms temperature fluctuations (right panel) as a function of height, in strong-field and weak-field regions, respectively: As the left panel shows, horizontal flows are stronger outside magnetic field concentrations than inside below $z = 400 \text{ km}$, and reach a maximum around $z = 200 \text{ km}$ where the granular upflows turn over and converge horizontally towards the downflow lanes. Above $z = 400 \text{ km}$ a different picture is obtained: the rms horizontal velocity inside magnetic structures *increases* with height, while the velocities outside decrease significantly. As a result, horizontal flows have larger amplitudes *inside* magnetic fields. Above $z = 500 \text{ km}$ these flows are accompanied by temperature fluctuations which clearly exceed the fluctuations outside magnetic fields (Fig. 4, right panel).

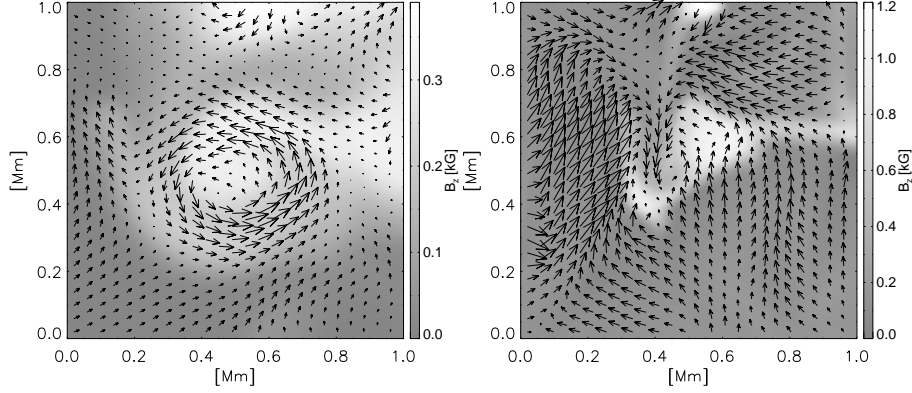


Figure 5: Detailed view of the flow and magnetic structure of a flux concentration. Left: vectors of horizontal velocity superimposed on a greyscale map of the vertical magnetic field at a height of 550 km above the visible surface. Right: the same at a height of 100 km. The longest arrows correspond to a velocity of 7 km s^{-1} .

As the example shown in Fig. 5 illustrates, one observes a correlation between flows inside magnetic structures at large heights and converging granular flows immediately outside magnetic structures at deeper levels near the visible surface around $\tau_{5000} = 1$. The anticlockwise whirl flow at $z = 550 \text{ km}$ (left panel) corresponds to a net circulation of granular flows around the magnetic element with the same orientation at $z = 100 \text{ km}$ (right panel). It is conceivable that the shear due to such surrounding flows excites torsional Alfvén waves which propagate upward along field concentrations. While the behaviour of such waves in the upper most parts of the computational domain can not be expected to be described realistically with closed upper boundary conditions, future versions of our code with a transmitting upper boundary will allow us to thoroughly analyze this potentially important mechanism of vertical energy transport and assess its relevance for the energy balance in the upper layers of the solar atmosphere.

3.2 Relation between brightness and magnetic field strength

It is a well established observational fact that the brightness of magnetic structures in the photosphere strongly depends on their size. While small field concentrations appear as bright points in intensity pictures, larger structures like pores and sunspots appear dark as a result of the reduced convective energy transport in their interior (see e.g. Zwaan 1987 for an overview of the hierarchy of magnetic elements). While the relation between brightness and magnetic field of small photospheric elements has been extensively studied theoretically in two-dimensional MHD simulations (e.g. Deinzer et al. 1984a,b, Steiner et al. 1998, Grossmann-Doerth et al. 1998), the simulation discussed

here also includes the transition to the regime of darker pore-like structures with diameters of the order of 1000 km.

As a comparison of the map of magnetic field strength with the intensity

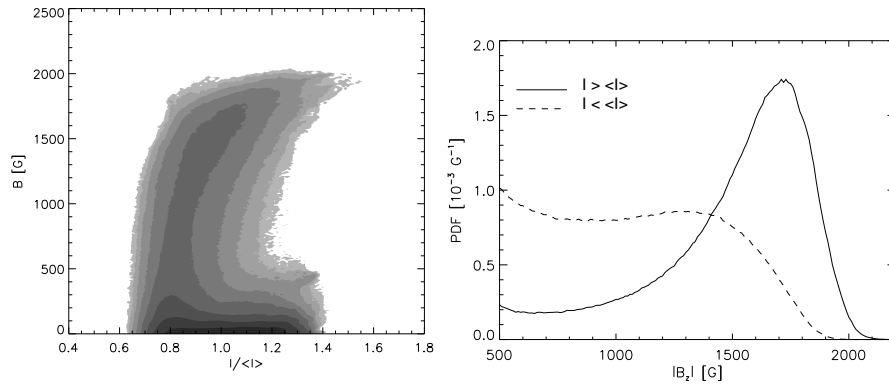


Figure 6: Left: joint probability distribution of magnetic field strength and brightness. The grey-shading indicates the probability density, with level-intervals of 0.5 on the \log_{10} -scale. Right: Probability distribution functions of the magnetic field strength inside the magnetic network ($|B_z| > 500$ G), for regions brighter and darker than average, respectively.

picture in Fig. 2 shows, the brightest magnetic structures are typically found in regions of high field strength of the order of 2000 G at $z = 0$. However, not all strong-field features stand out as particularly bright; larger structures with extended regions of magnetic fields above 1000 G tend to appear darker than average. This impression is confirmed quantitatively by Fig. 6. The left panel shows the joint PDF of magnetic field strength at $z = 0$ and emergent intensity, based on simulation data of approximately one hour simulated time. While a large part of the magnetic regions has an intensity below the average value, the largest field strengths show a trend towards increased brightness, with maximum intensities exceeding those of bright nonmagnetic regions (i.e., granules). The right panel shows the probability distribution of magnetic field strength in bright (solid line) and dark (dashed line) magnetic regions, both curves being separately normalized to unity. While the fields with below-average brightness have a rather flat distribution up to fields of 1500 G, the distribution for the bright features shows a steep increase with increasing field strength and reaches a pronounced maximum at 1700 G.

Figures 7 and 8 allow a closer look at a typical sheet-like structure which illustrates the connection between brightness and field strength in more detail. Fig. 7 shows magnetic field and intensity maps of a typical bright, elongated magnetic structure embedded in a dark downflow lane. The straight line marks the position of the vertical cut through this structure shown in Fig. 8. As Fig. 8 illustrates, the partial evacuation of the magnetic structure leads

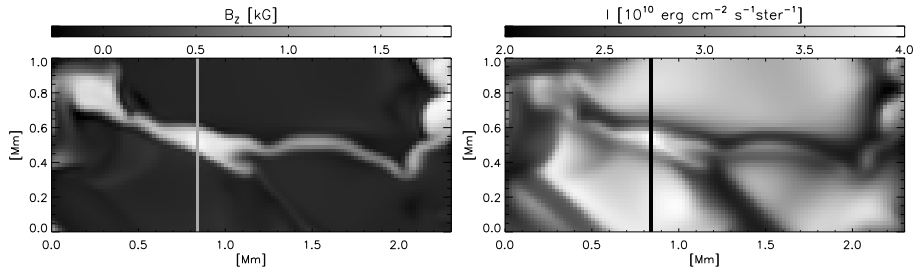


Figure 7: Vertical field strength at $z = 0$ (left) and intensity map (right) for a sheet-like magnetic structure. The solid lines indicate the position of the cut shown in Fig. 8.

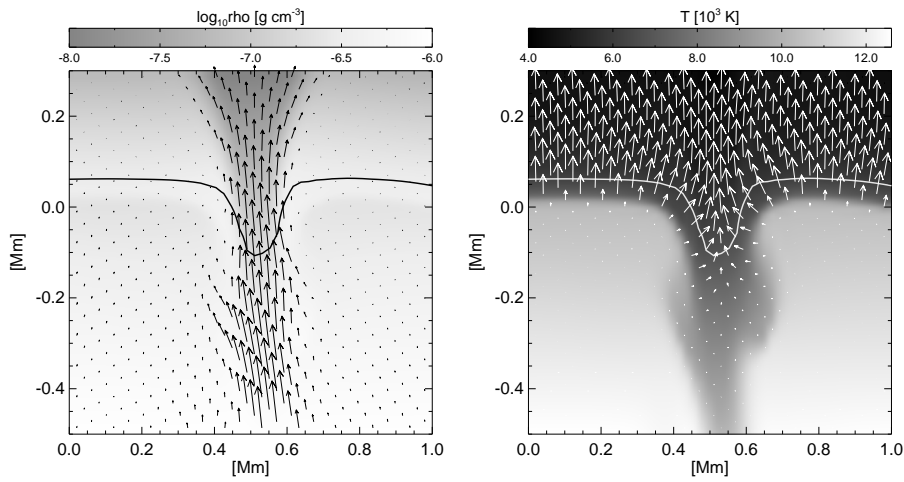


Figure 8: Vertical cut through the sheet-like magnetic structure shown in Fig. 7. Left panel: Density structure and magnetic field vectors projected on the plane of view. The longest vector corresponds to a field strength of 2000 G. Right panel: temperature structure and radiative flux vectors. The solid lines indicate the level $\tau_{\text{Ross}} = 1$.

to a depression of the visible surface inside the sheet (the bold solid lines, indicating the level $\tau_{\text{Ross}} = 1$). This results in radiation flowing in from the hot neighbouring granules through the sidewalls, heating up the interior of the sheet. This horizontal heating is balanced by cooling due to radiative losses in the vertical direction. The resulting net radiative heating rate in the interior of the sheet is very small which indicates that almost no conversion from convective to radiative energy transport takes place inside the structure where the magnetic field is dynamically relevant. The bright appearance of the sheet is, in turn, a direct consequence of the increased temperature around the (depressed) visible surface corresponding to this radiative equilibrium.

This example confirms the basic mechanism for brightness enhancement that was already found in earlier, more simplified models of photospheric magnetic elements (e.g. Deinzer et al. 1984a,b, Knölker et al. 1988) and demonstrates that results of idealized, two-dimensional models are indeed relevant for the explanation of some aspects of three-dimensional magnetoconvection.

It should be noted that radiative heating is not the only mechanism which has an influence on the temperature structure of magnetic structures. In principle, Joule dissipation near the edges of the magnetic sheet, where the gradients in field strength are large, can also heat up the interior of the sheet. In the solar photosphere, this effect is expected to be small compared with the radiative heat influx because of the high electric conductivity of the plasma. Since the value of the conductivity in simulations of this kind is unrealistically low – an inevitable consequence of the limited spatial resolution – Joule heating tends to be overestimated. However, as a thorough analysis shows, the contribution of Joule dissipation to the total heating around $\tau = 1$ is negligible, indicating that the effects of limited grid resolution do not seriously affect the temperature structure obtained from the simulation.

4 Magneto-convection for different amounts of flux

Magneto-convection in the solar photosphere is observed in a variety of regimes, which are mainly characterized by the average magnetic field, B_0 , corresponding to the amount of magnetic flux per unit area in the region considered. The average field strength spans a range from 10 G in the quiet Sun to up to 3000 G in sunspot umbrae. The simulation discussed in the previous section is part of an ongoing parameter study to investigate the properties of photospheric magneto-convection and their dependence on the average magnetic field strength, B_0 . In this section, we give a brief overview of simulation runs with $B_0 = 10, 50, 200, 400,$ and 800 G, respectively. In all cases, box size and grid resolution are identical to the setup described in Sect. 3. Figs. 9 and 10 show the vertical magnetic field and vertical velocity on a horizontal plane near $\langle\tau_{500}\rangle = 1$ together with the frequency-integrated brightness, for the five simulation runs considered here. The run with $B_0 = 10$ G shows nearly undisturbed granulation. Several predominantly vertical flux concen-

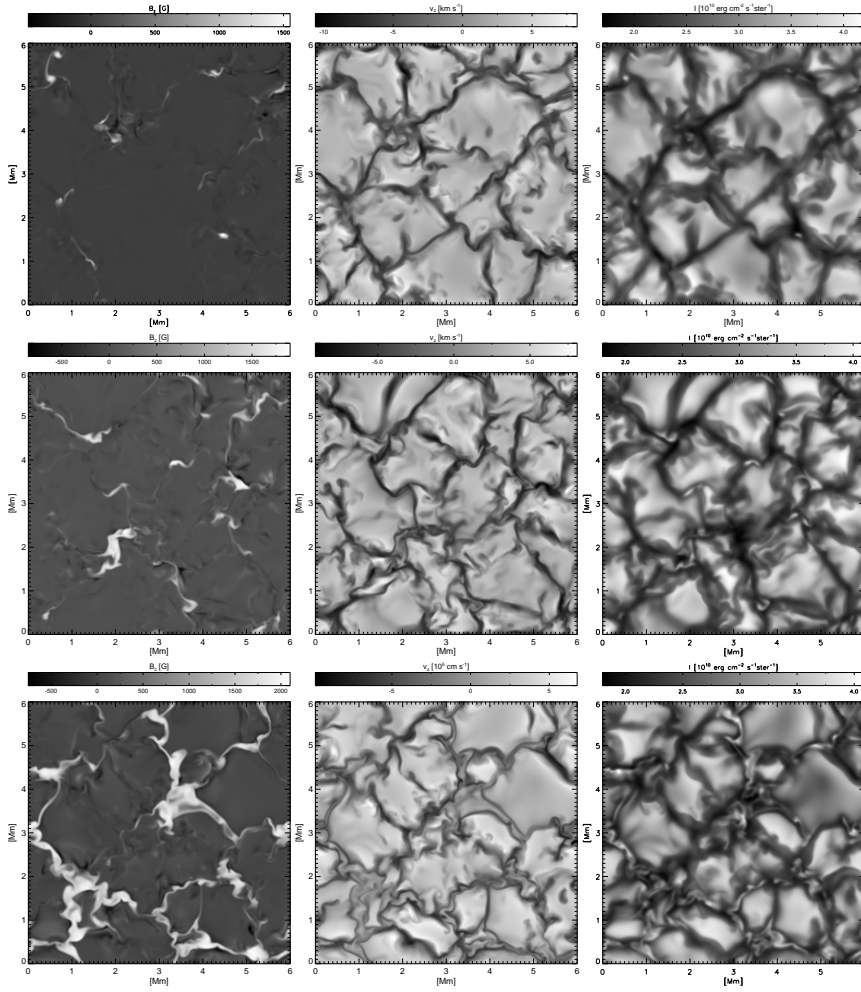


Figure 9: Snapshots from simulation runs with $B_0 = 10$ G (top row), $B_0 = 50$ G (second row), and $B_0 = 200$ G (bottom row). Shown are horizontal cuts near the visible solar surface of the vertical magnetic field (left column), vertical velocity (middle column, up- and downflows are indicated by light and dark shades, respectively), and brightness (frequency-integrated radiation intensity, right column). See also Fig. 10 for the cases with $B_0 = 400$ G and $B_0 = 800$ G.

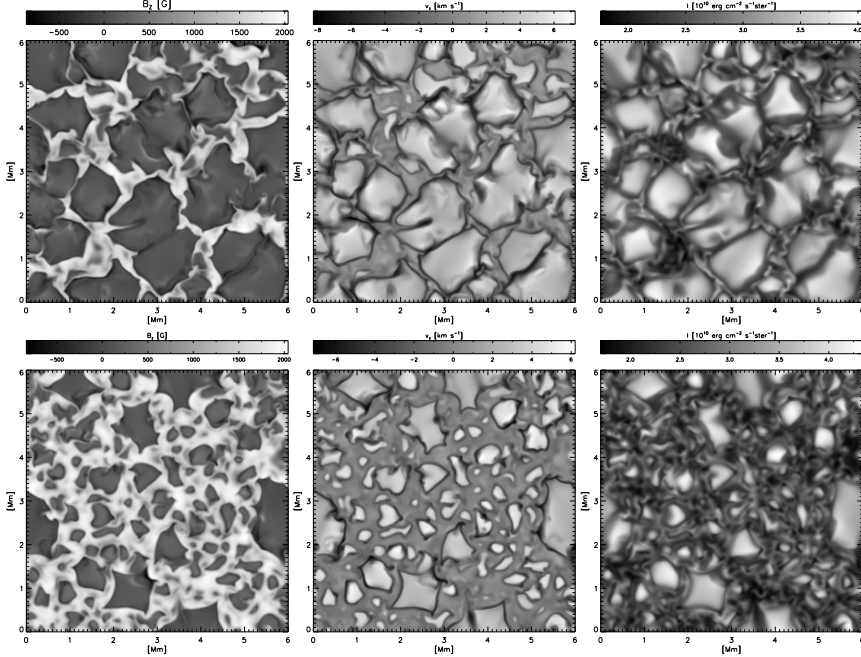


Figure 10: Same as Fig. 9, for $B_0 = 400$ G (upper panels), and $B_0 = 800$ G (lower panels).

trations with a maximum field strength of up to 1700 G have formed in the network downflows and appear in the form of bright points in the dark intergranular lanes. With growing B_0 , strong field concentrations occupy an increasing fraction of the area, and the granular pattern becomes more and more affected by the field, the average granule size shrinking as the network of magnetic fields in the kilogauss range becomes a quasi-impenetrable obstacle for horizontal flows. Owing to the brightness enhancement of smaller field concentrations discussed in the previous section, the brightness of a considerable part of the area between granules is lifted above the intensity level of nonmagnetic downflows, and, consequently, the root-mean-square intensity contrast of the granulation is reduced from 18% in the “quiet Sun” run with $B_0 = 10$ G to approximately 15% for $B_0 = 200$ G and larger. The disturbance of the granular pattern becomes rather severe in the case $B_0 = 800$ G. Here the dynamic backreaction of the magnetic field on the convective flows leads to the formation of numerous small upflows with typical diameters of 200 – 500 km. A smaller number of larger, more vigorous upflows penetrates the magnetic network and appear as isolated bright dots against a dark background of almost stagnant, strongly magnetized plasma – a situation reminiscent of the case of a sunspot umbra interspersed with umbral dots.

In all five cases, the strongest fields clearly exceed the equipartition value

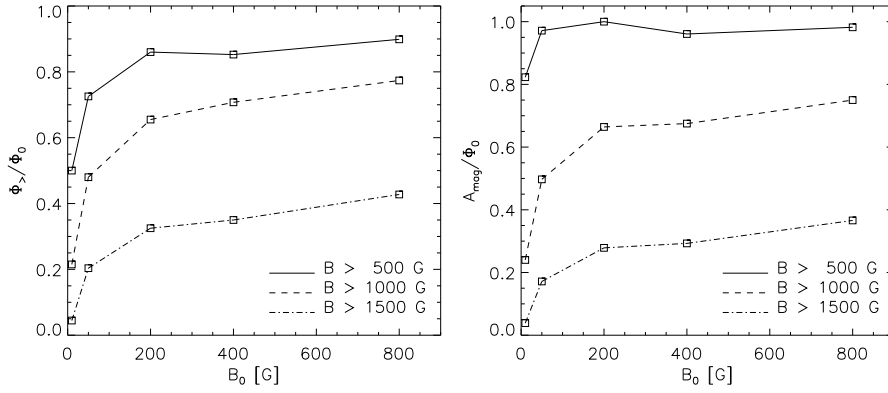


Figure 11: Left panel: the curves show the fraction of the total surface flux stored in fields stonger than, respectively, 500 G, 1000 G, and 1500 G, as a function of the average field strength, B_0 . Right panel: ratio between the fractional area occupied by fields stonger than field strength B (for $B = 500$ G, 1000 G, and 1500 G), A_{mag} , and the total surface flux, Φ_0 , as a function of B_0 (the unit for A_{mag}/Φ_0 is arbitrary).

of 400 – 500 G in our simulations, the maximum field strength growing moderately from approximately 1700 G for $B_0 = 10$ G to 2200 G for $B_0 = 800$ G. The distribution of the surface flux over the range of field strengths, however, undergoes a more pronounced change. The left panel of Fig. 11 shows, as function of the average field strength, B_0 , the fraction of the total surface flux stored in fields exceeding a certain threshold field strength B_t , for $B_t = 500$ G, 1000 G, and 1500 G, respectively. For all three values of B_t , the fractional flux $\Phi_{>}/\Phi_0$ strongly increases with B_0 for $B_0 \leq 200$ G. Beyond $B_0 = 200$ G the dependence of $\Phi_{>}/\Phi_0$ on B_0 is much weaker. For the simulation runs with $B_0 = 200$ G, 400 G, and 800 G, between 85% and 90% of the total flux has field strength larger than the equipartition value of 500 G. The fraction decreases significantly for smaller B_0 , but still about 50% of the flux is in superequipartition state for the “quiet Sun” run with $B_0 = 10$ G. For larger threshold values B_t , the drop of $\Phi_{>}/\Phi_0$ with decreasing average field strength is more drastic, indicating that the efficiency of convective field intensification to values significantly higher than the equipartition level is strongly reduced in the case of small average field strengths corresponding to quiet Sun conditions.

The right panel of Fig. 11 shows the ratio between the area A_{mag} occupied by strong fields exceeding field strength B_t and the total flux, Φ_0 (in arbitrary units), as a function of B_0 . For $B_t = 500$ G, the curve is almost flat, which indicates that the area covered by fields with at least equipartition strength scales linearly with the total flux. So, independently of average field strength and corresponding efficiency of producing kilogauss fields, convective flows amplify a certain fraction of the total flux to equipartition level,

the probability of occurrence *per mean flux* being more or less the same for quiet Sun and active region conditions. For $B_t = 1000$ G and 1500 G, the strong decrease of the ratio A_{mag}/Φ_0 for small B_0 reflects the low probability for the occurrence of kilogauss fields in magnetic maps of quiet Sun simulations. The finding that the flux in superequipartition form grows faster than the occupied area with increasing B_0 for $B_0 \lesssim 200$ G, implies that the average field strength of strong field concentrations also increases significantly with B_0 for $B_0 \lesssim 200$. The fact that for small total flux the strong fields preferentially occur in form of more or less isolated flux concentrations whose typical size grows with increasing B_0 (as can be inferred from the magnetic maps in Fig. 9), suggests an interpretation of this result along the lines of Venkatakrishnan (1986) who predicted that, owing to efficient radiative heating by the surrounding gas, convective field intensification to field strengths significantly larger than equipartition is less efficient for smaller flux tubes. Our simulations are also in good agreement with observations by Solanki et al. (1996) who found that the intrinsic field strength of small quiet Sun flux concentrations (with $\Phi \lesssim 10^{17}$ Mx) increases strongly with their size, while it becomes almost size-independent for larger magnetic features.

Acknowledgements

I would like to thank Manfred Schüssler for many helpful comments and fruitful discussions. I am grateful to Sergey Shelyag, Fausto Cattaneo, Thierry Emonet and Timur Linde for their contributions to the development of the MURaM code. This work was supported by the Max-Planck-Institut für Sonnensystemforschung through a doctoral stipend and by the DFG through grant SCHU 500/7.

References

- Cattaneo, F., Lenz, D., Weiss, N. 2001, ApJ 563, L91
 Caunt, S. E., Korpi, M. J. 2001, A&A, 369, 706
 Deinzer, W., Hensler, G., Schüssler, M., Weishaar, E. 1984, A&A 139, 426
 Deinzer, W., Hensler, G., Schüssler, M., Weishaar, E. 1984, A&A 139, 435
 Dunn, R.B., Zirker, J.B. 1973, Sol. Phys. 33, 281
 Grossmann-Doerth, U., Schüssler, M., Solanki, S.K. 1989, A&A 221, 338
 Grossmann-Doerth, U., Schüssler, M., Steiner, O. 1998, A&A 337, 928
 Knölker, M., Schüssler, M., Weishaar, E. 1988, A&A 194, 257
 Knölker, M., Grossmann-Doerth, U., Schüssler, M., Weishaar, E. 1991 Advances in Space Research 11, 285
 Kunasz, P. B., Auer, L. 1988, J. Quant. Spectr. Radiat. Transfer, 39, 67
 Ludwig, H. G. 1992, PhD Thesis, Universität Kiel
 Nordlund, A. 1982, A&A, 107, 1

- Proctor, M.R.E. 1992, in: J.H. Thomas, N.O. Weiss (eds.), *Sunspots, Theory and Observations*, NATO ASI C375, Kluwer, p.221
- Proctor, M.R.E., Weiss, N.O. 1982, Rep. Prog. Phys. 45, 1317
- Rast, M. P., Nordlund, A., Stein, R. F. , Toomre, J. 1993, ApJ 408, L53-L56
- Rast, M. P., Toomre, J. 1993, ApJ 419, 224
- Schüssler M. 2001, in M. Sigwarth (ed.), *Advanced Solar Polarimetry – Theory, Observation, and Instrumentation*, ASP Conf. Ser. 236, 343
- Schüssler M., Knölker M. 2001, in G. Mathys, S.K. Solanki, D.T. Wickramasinghe (eds.), *Magnetic Fields Across the Hertzsprung-Russell Diagram*, ASP Conf. Ser. 248, 115
- Sigwarth, M., Balasubramaniam, K.S., Knölker, M., Schmidt, W. 1999, A&A 349, 941
- Solanki, S.K., 1989, A&A 224, 225
- Solanki, S.K., Zufferey, D., Lin, H., Rüedi, I., Kuhn, J.R. 1996, A&A 310, L33
- Steiner, O., Grossmann-Doerth, U., Knölker, M., Schüssler, M. 1998, ApJ 495, 468
- Venkatakrishnan, P. 1986, Nat. 322, 156
- Vögler, A., Bruls, J.H.M.J, Schüssler, M. 2004, A&A, in press
- Weiss, N.O. 1997, in *1st Advances in Solar Physics Euroconference. Advances in Physics of Sunspots*, ASP Conf. Ser. 118,21
- Zwaan, C. 1987, Ann. Rev. Astron. Astroph., 25, 83